Available online at www.sciencedirect.com
SCIENCE DIRECT®
ELSEVIER
International Journal of Solids and Structures 41 (2004) 6573–6596
INTERNATIONAL JOURNAL OF SOLIDS and STRUCTURES
www.elsevier.com/locate/ijsolstr

Stochastic fracture of ceramics under dynamic tensile loading

Fenghua Zhou, Jean-Francois Molinari *

Department of Mechanical Engineering, Johns Hopkins University, 232 Latrobe Hall, 3400 N. Charles Street, Baltimore, MD 21218, USA

Received 13 March 2003; received in revised form 11 May 2004
Available online 20 July 2004

Abstract

Three-dimensional numerical simulations are performed to investigate the dynamic tensile properties of ceramics, using explicit dynamic FEM and cohesive element techniques. A micro-cracking model considering the stochastic distribution of internal defects is developed. The model consists of a Weibull distribution of the local strengths, and a facet area modification that accounts for the equivalent geometry of the elements. Preliminary calculations are performed to verify the capability of this model in addressing mesh-dependency. The calculations show that the brittleness of the material tends to deteriorate the mesh-dependency problem. However, by using the equivalent geometry modification with adequate parameters, the unwanted mesh-dependency can be satisfactorily corrected. Parametric studies are performed to investigate the influences of the fracture energy and Weibull modulus. It is seen that for a fixed loading speed, the strength of the specimen increases with the fracture energy, but decreases when the material becomes more heterogeneous. The scatter of specimen strengths decreases when the material becomes more ductile. The observed phenomena are explained by the micro-cracking mechanism of ceramics failure. The effect of loading speed is also investigated, significant rate-hardening effect is observed. It is shown that the micro-cracking mechanism, which is different in the dynamic loading case and static loading case, can explain the observed rate-dependency of the ceramic tensile strength.

Keywords: Dynamic fracture; Ceramics; Stochastic property; Numerical simulation; Micro-cracking mechanism; Mesh-dependency; Rate-hardening

1. Introduction

Ceramics are good material candidates for armor applications because of their hardness and lightweight. When designing an armor system, it is important to understand the mechanical properties of ceramics under strong, high rate impact loading. In order to develop the constitutive models to describe the deformation and failure properties under impact loading, extensive research has been performed experimentally using the Split Hopkinson Pressure Bar (SHPB) technique (e.g., Chen and Ravichandran, 1997,

* Corresponding author. Tel.: +1-410-516-2864; fax: +1-410-516-7254.
E-mail address: molinari@jhu.edu (J.-F. Molinari).

0020-7683/$ - see front matter © 2004 Published by Elsevier Ltd.
doi:10.1016/j.ijsolstr.2004.05.029

2000; Shih et al., 2000; Subhash and Ravichandran, 1998; Sarva and Nemat-Nasser, 2001; Jiao et al., 2004; Wang and Ramesh, 2004) or plate impact technique (e.g., Grady, 1997; Bourne et al., 1998). It was found that the failure strength and the failure mode of the ceramics are highly dependent on the lateral confinement; while the rate-sensitivity of the strength can be either high or moderate depending on materials and strain-rate regions. The experimental work showed that the microscopic defects significantly influence the strength and failure mode of the material.

Different theoretical models have been proposed based on the experimental observations. The micro-crack-nucleation-growth model of Ravichandran and Subhash (1995), and the energy-diffusion model of Bhattacharya et al. (1998), are two representative ones. Both models use mathematical analysis to describe the failure process of ceramics. In the model of Ravichandran and Subhash, the propagation behavior of a micro-crack (source of damage) within a confined cell is investigated; the failure of the bulk material is defined as the instance when the damage density reaches a critical value. In the model of Bhattacharya et al., the elastic energy within an intact specimen and a slit (failed) specimen are calculated by a macroscopic approach; the criterion for specimen failure is that the reduction of the elastic energy from *intact* state to the *split* state must overcome the surface energy associated with the newly created surfaces. The experimental observations about failure strength dependency on the confining pressure are successfully explained by Bhattacharya et al.'s energy model.

Though a mechanics based analyzing model can provide elementary interpretations about the failure mechanism, the dynamic failure process of ceramics is often too complex to be formulated theoretically. Ceramics are usually brittle and have many intrinsic defects. The existence of these initial defects brings in the stochastic strength properties of the bulk material. Under dynamic loading, these defects may nucleate to form many micro-cracks, which result in the fragmentation of the material. Moreover, the high-speed crack growth process is always accompanied with the inertia effect and rate-dependent fracture process. To account for most of the mechanisms, numerical simulation is the exclusively promising method. In the models proposed by different authors (Camacho and Ortiz, 1996; Espinosa et al., 1998; Miller et al., 1999; Zhai and Zhou, 2000; Zavattieri and Espinosa, 2001; Zavattieri et al., 2001), the dynamic failure process is simulated by the nucleation and the growth of micro-cracks within the ordinary element boundaries. The propagation behaviors of these micro-cracks are simulated by cohesive elements. All these simulations are two-dimensional. The core part of these simulations is the modeling of micro-cracks. This is performed by using the cohesive elements. Cohesive elements are derived from the cohesive zone concept, which was introduced by Dugdale (1960) and Barrenblatt (1962). The cohesive zone implementation into numerical analysis is the cohesive element, which explicitly simulates crack propagation. The work of Xu and Needleman (1994, 1996), Camacho and Ortiz (1996) demonstrated successful use of the cohesive element in two-dimensional cases. The work of Ortiz and Pandolfi (1999), Pandolfi et al. (1999, 2000), and Ruiz et al. (2000, 2001) successfully implemented cohesive elements into three-dimensional analysis in a range of applications. In this paper, we will adopt a similar strategy, to perform *three-dimensional* numerical simulations by an explicit finite element analysis package incorporating a cohesive-element capability. Several simulations of the dynamic fracture phenomena have been conducted to verify and validate this methodology (Zhou and Molinari, 2001).

A major difficulty that arises in a three-dimensional simulation is the size of the problem. Due to the limitations in computational capabilities, a three-dimensional simulation cannot be too large. This often leads to mesh-dependency problem. In our previous work (Zhou and Molinari, 2004), we have developed a dynamic three-dimensional FEM technique to investigate the fracture/fragmentation behavior of brittle structures. In the simulations, the brittle structures are considered as bodies containing initial defects. These defects are modeled as the facets shared by two neighboring ordinary elements. Each facet has a specified strength and fracture energy. When the loading stress on the facet exceeds its strength, the facet will be activated as a micro-crack that is treated as a cohesive element. Because the cohesive elements are inserted into ordinary elements dynamically (following the method of Pandolfi and Ortiz, 2002), the problem size is

minimized. The strengths of the facets are scattered and observe a Weibull distribution. One immediate benefits of using this model is that due to the effective-volume concept of the Weibull theory, the undesirable mesh-dependency of the numerical calculation is significantly reduced.

The modeling technique was applied to analyze the failure processes of a ceramic (Silicon carbide, SiC) cube under impact loading (Zhou and Molinari, 2003). An effective-shear-stress criterion of micro-crack initiation and a frictional contact algorithm was incorporated into the cohesive element procedures. The specimen under different loading rates was numerically tested to determine the compressive strengths of the specimen. It was found that the strain-rate has moderate influence on the average strength of the specimen. We have also investigated the influence of transversal confinement on the compressive strength. It was shown that the confining pressure significantly increases the failure strength of the specimen. The simulation results were in good agreement with experimental observations.

In this paper, we study the failure process of a SiC specimen under dynamic *tensile* loading. Due to the testing difficulties such as gripping and specimen alignment, little experimental results have been found for this problem (Walter et al., 1994). The numerical simulations intend to provide elementary intuitions on the phenomenon. The material is assumed to contain Weibull distributed initial defects; therefore the failure mode is stochastic. The failure of the specimen is simulated by the nucleation and the propagation of these micro-cracks. The intrinsic damage scale (having the order of element size) is much smaller than the specimen scale. A brittle system and a ductile system, with different fracture energy, are considered in the analysis. We will show that for these two systems, the damage-scale stochastic properties influence the specimen-scale strength properties differently.

We start this paper by describing the explicit FE implementation as well as cohesive element technique (Section 2). Then, the microscopic stochastic fracture model including a Weibull strength distribution and an equivalent area modification are detailed (Section 3). The application phase contains three sections. In Section 4 we use four meshes, each having different element sizes, to calculate the tensile strength of a ceramic specimen. The simulation results are dependent on the mesh type (mesh-dependency), especially for the brittle system. We show that by introducing a Weibull-type strength modification and using appropriate parameters, the mesh-dependency can be efficiently controlled. In Section 5, we fix the mesh and the loading speed, to conduct parametric studies on material properties. It is shown that the strength of the specimen varies with the initial distribution of defects, and the fracture energy. The physical reasons for these phenomena are discussed. In Section 6, we extensively study the dynamic failure characteristics of a brittle and a ductile specimen. A remarkable finding is that both the brittle system and the ductile system show strong rate-sensitivity, which is different from the compression-failure phenomenon. An energy-dissipation theory based on micro-cracking mechanism is proposed to explain the apparent rate-dependency observations. The conclusions and discussions are made in Section 7.

2. Finite element methodology and cohesive element

2.1. Equations of continuum mechanics

Following the methodology outlined by Molinari and Ortiz (2002), we consider the general case of a body occupying an initial configuration $B_0 \subset \mathbf{R}^3$ of the body at time t_0. We select B_0 as the reference configuration. The motion of the body is described by a time-dependent deformation mapping φ: $B_0 \times [t_0, T] \to \mathbf{R}^3$. The initial deformation mapping, $\varphi(0)$ and the material velocity field, $\dot{\varphi}(0)$, are supplied to formulate the problem.

At an arbitrary time t, the local deformation of infinitesimal material neighborhoods is described by the deformation gradient

$$\mathbf{F} = \nabla_0 \varphi, \quad \text{in } B_0 \tag{1}$$

where ∇_0 denotes the material gradient over B_0.

For purposes of formulating boundary conditions, we partition the boundary ∂B_0 of B_0 into a displacement boundary ∂B_{01} and a traction boundary ∂B_{02}. The displacement boundary conditions take the form:

$$\varphi = \bar{\varphi}(\mathbf{X}, t), \quad \text{on } \partial B_{01} \tag{2}$$

where $\bar{\varphi}(\mathbf{X}, t)$ is the prescribed deformation mapping on ∂B_{01}. The traction boundary conditions take the form:

$$\mathbf{P} \cdot \mathbf{N} = \bar{\mathbf{t}}(\mathbf{X}, t), \quad \text{on } \partial B_{02} \tag{3}$$

where $\boldsymbol{P}$ is the first Piola–Kirchhoff stress, $\boldsymbol{N}$ is the unit outward normal to ∂B_{02} and $\bar{\mathbf{t}}(\mathbf{X}, t)$ is the prescribed tractions applied on ∂B_{02}.

In addition, the solids contain a collection of cohesive cracks. We denote the location of these cracks by S_0 which has the unit of area. The cohesive surface leads to a new term in the principle of virtual work.

Under these conditions, the weak form of linear momentum balance takes the form:

$$\int_{B_0} [\rho_0(\mathbf{b} - \ddot{\varphi}) \cdot \boldsymbol{\eta} - \mathbf{P} \cdot \nabla_0 \boldsymbol{\eta}] \mathrm{d}V_0 - \int_{S_0} \mathbf{t} \cdot \|\boldsymbol{\eta}\| \mathrm{d}S_0 + \int_{\partial B_{02}} \bar{\mathbf{t}} \cdot \boldsymbol{\eta} \, \mathrm{d}S_0 = 0 \tag{4}$$

where a superposed dot denotes the material time derivative, $\boldsymbol{\eta}$ is an admissible virtual displacement satisfying homogeneous boundary conditions on ∂B_{01}, $\boldsymbol{t}$ is the cohesive traction, $\rho_0 \boldsymbol{b}$ are the body forces, and $\|\|$ denotes the jump across an oriented surface.

2.2. Cohesive law: general forms

The ceramics under loading are considered as a bulk material including cracks. Two sets of constitutive equations are needed for the simulation: one describes the mechanical behavior of the bulk material; the other describes the cohesive behavior of the crack. As the ceramics are brittle, we use homogeneous, isotropic elasticity to describe the bulk material. For the crack behavior, we use the cohesive model developed by Camacho and Ortiz (1996), Ortiz and Pandolfi (1999), Pandolfi et al. (1999, 2000). Following their methodology, we postulate the existence of a free energy density per unit area of crack, ϕ, which takes the form:

$$\phi = \phi(\boldsymbol{\delta}, \theta, \mathbf{q}; \mathbf{n}) \tag{5}$$

where

$$\boldsymbol{\delta} = \|\varphi\| \tag{6}$$

is the opening displacement over the cohesive surface, θ is the local temperature, $\boldsymbol{q}$ is some appropriate collection of internal variables, which describe the inelastic processes attendant to decohesion, and $\boldsymbol{n}$ is the unit normal vector of the cohesive surface in the deformed configuration. The explicit dependence of ϕ on $\boldsymbol{n}$ is required to allow for the differences in cohesive behavior for opening and sliding. The cohesive law, which defines the function between the cohesive traction $\boldsymbol{t}$ and the opening displacement $\boldsymbol{\delta}$, is given by:

$$\mathbf{t} = \frac{\partial \phi}{\partial \boldsymbol{\delta}} \tag{7}$$

The potential structure of the cohesive law is a consequence of the first and second laws of thermodynamics. We consider a simple class of mixed-mode cohesive laws accounting for tension-shear coupling obtained by the introduction of an effective opening displacement, δ_{eff}, defined as:

$$\delta_{\text{eff}} = \sqrt{\beta^2 \delta_{\text{s}}^2 + \delta_{\text{n}}^2} \tag{8}$$

where

$$\delta_{\text{n}} = \boldsymbol{\delta} \cdot \mathbf{n} \tag{9}$$

is the normal opening displacement, and

$$\delta_{\text{s}} = |\boldsymbol{\delta}_{\text{s}}| = |\boldsymbol{\delta} - \delta_{\text{n}} \cdot \mathbf{n}| \tag{10}$$

is the magnitude of sliding displacement. The parameter β assigns different weights to the sliding and normal opening displacements.

Assuming that the free energy potential ϕ depends on $\boldsymbol{\delta}$ only through the effective opening displacement, δ_{eff}, i.e.

$$\phi = \phi(\delta_{\text{eff}}, \theta, \mathbf{q}) \tag{11}$$

the cohesive law reduces to

$$\mathbf{t} = \frac{t_{\text{eff}}}{\delta_{\text{eff}}} (\beta^2 \boldsymbol{\delta}_{\text{s}} + \delta_{\text{n}} \mathbf{n}) \tag{12}$$

where

$$t_{\text{eff}} = \frac{\partial \phi(\delta_{\text{eff}}, \theta, \mathbf{q})}{\partial \delta_{\text{eff}}} \tag{13}$$

is a scalar effective traction, which can be shown to be equal to:

$$t_{\text{eff}} = \sqrt{\beta^{-2} |\mathbf{t}_{\text{s}}|^2 + t_{\text{n}}^2} \tag{14}$$

where $\mathbf{t}_{\text{s}}$ and t_{n} are the shear and normal tractions. It is seen that the parameter β defines the ratio between shear and normal tractions.

2.3. Linear irreversible cohesive law

In our simulation we omit the effect of local temperature θ. For the form of the cohesive law $t_{\text{eff}}(\delta_{\text{eff}})$, we have found that the maximum traction and the fracture energy are important parameters. However, the shape of $t_{\text{eff}}(\delta_{\text{eff}})$ function has little influence on the final results (Zhou and Molinari, 2001). Following Camacho and Ortiz (1996), we use the simple irreversible, linear decaying function for the constitutive behavior of the cohesive elements. This cohesive law is specifically adequate for the numerical scheme in which cohesive elements are dynamically added to the structure. The law is shown in Fig. 1. Irreversibility signifies that the damage in a given cohesive element cannot be recovered. The cohesive law is expressed as:

$$\begin{aligned} &\frac{t_{\text{eff}}}{\sigma_{\text{c}}} = 1 - \frac{\delta_{\text{eff}}}{\delta_{\text{c}}}, \quad \text{for } \dot{\delta}_{\text{eff}} > 0, \quad \delta_{\text{eff}} = \delta_{\max} \\ &\frac{t_{\text{eff}}}{\sigma_{\text{c}}} = \frac{\delta_{\text{eff}}}{\delta_{\max}} - \frac{\delta_{\text{eff}}}{\delta_{\text{c}}}, \quad \text{for } \delta_{\text{eff}} < \delta_{\max} \end{aligned} \tag{15}$$

where σ_{c} is the maximum cohesive force and δ_{c} is the critical opening distance. The parameters $(\sigma_{\text{c}}, \delta_{\text{c}})$ constitute the material data that characterizes fracture: σ_{c} can be viewed as the microscopic strength of the materials, and δ_{c} the microscopic CTOD beyond which a surface is fully opened and retains no cohesion. The area under the curve of Fig. 1 is the fracture energy that is needed to fully open a unit area of crack surface:

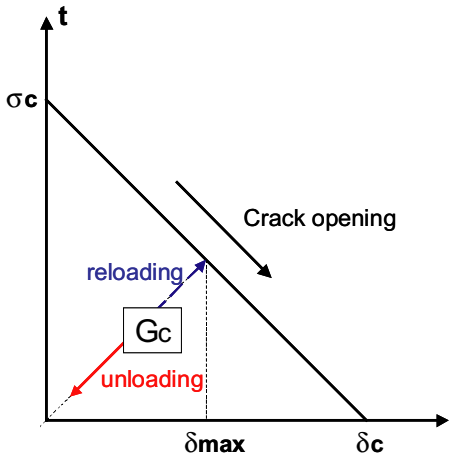

Fig. 1. Irreversible linear decaying cohesive law.

$$G_c = 2\Gamma_c = \frac{\sigma_c \delta_c}{2} \tag{16}$$

where G_c is the fracture energy, Γ_c is the surface energy.

2.4. Explicit dynamic finite element analysis

Upon discretization, the principle of the virtual work applied to the equilibrium equation (4) renders:

$$\mathbf{M}\ddot{\varphi} + \mathbf{R}^{\text{int}}(\varphi) = \mathbf{R}^{\text{ext}}(t) \tag{17}$$

where $\mathbf{R}^{\text{ext}}$ and $\mathbf{R}^{\text{int}}$ are the external and internal forces arrays, $\mathbf{M}$ is the mass matrix, and φ is the nodal coordinates array.

This equation is integrated along the time axis by the Newmark scheme. The second-order accurate explicit scheme, an explicit version of the Newmark scheme, are shown as following (see Belytschko, 1983; Hughes, 1987):

$$\varphi_{n+1} = \varphi_n + \Delta t \mathbf{v}_n + \frac{1}{2}\Delta t^2 \mathbf{a}_n \tag{18}$$

$$\mathbf{a}_{n+1} = \mathbf{M}^{-1}(\mathbf{R}^{\text{ext}}_{n+1} - \mathbf{R}^{\text{int}}_{n+1}) \tag{19}$$

$$\mathbf{v}_{n+1} = \mathbf{v}_n + \frac{1}{2}\Delta t(\mathbf{a}_n + \mathbf{a}_{n+1}) \tag{20}$$

where $\mathbf{v}$ and $\mathbf{a}$ are the material velocity and acceleration fields. Note that for explicit equation solving, the mass matrix $\mathbf{M}$ is lumped (diagonal). Therefore the reverse of it ($\mathbf{M}^{-1}$) is calculated immediately, and Eqs. (18)–(20) are solved explicitly.

To guarantee the stability of the time integration, the time step Δt must be lower than a critical value, Δt_{stable}, which is related to the dilatational (the fastest) wave speed and the (smallest) mesh size. In our simulation, the time step is taken as:

$$\Delta t = C\Delta t_{\text{stable}} = C \min_{\text{mesh}} \left(h^e \Big/ \sqrt{\frac{(1-v)E}{(1+v)(1-2v)}} \Big/ \rho \right) \tag{21}$$

where C is a security coefficient ($C < 1.0$), h^e is the dimension of the element, E, v and ρ are the Young's modulus, the Poisson ratio and the density of the material. The quantity $\sqrt{\frac{(1-v)E}{(1+v)(1-2v)}} \Big/ \rho$ is the wave speed of plane strain stress wave.

3. Microscopic cracking model

3.1. Ordinary elements and internal facets

We consider the failure process of a ceramic block under tensile loading. The block is divided by ordinary bulk elements. The interfaces between two neighboring elements, the facets, are treated as possible cracks, which may be activated to form the cohesive elements (Fig. 2).

Fig. 3a shows a 12-node cohesive element linked to two neighboring 10-node bulk elements. Note that at the beginning of the calculation, there is no cohesive element; namely, the material is crack free. Throughout the calculation the cohesive elements are inserted into the mesh *dynamically* : a cohesive element is created whenever, wherever the local effective traction acting on the facet reaches the cohesive strength of the material, i.e.,

$$\sigma_{\text{local}} = \sqrt{\beta^{-2}\tau^2 + \sigma_{\text{n}}^2} > \sigma_{\text{facet}} \tag{22}$$

where σ_{n} and τ are the normal and the shear traction applied on the facet (Fig. 3b), σ_{facet} is the local strength of the material.

When the criterion (22) is satisfied, a cohesive element is inserted between the two tetrahedral elements adaptively. The topology of the mesh is modified accordingly. The new created cohesive element has the cohesive parameters $\{\sigma_{\text{facet}}, \delta_{\text{facet}}\}$. After creation, the cohesive element behaves as a crack, which resists opening until it is fully damaged ($\delta_{\max} = \delta_{\text{facet}}$).

3.2. Distribution of facet strengths

For the brittle materials such as ceramics, the local cohesive parameters, σ_{facet} and δ_{facet}, are not necessarily constants because of the presence of intrinsic and extrinsic defects. To account for the stochastic

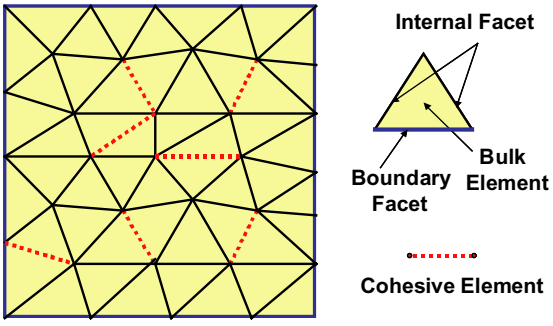

Fig. 2. Finite element discretization of a ceramic block.

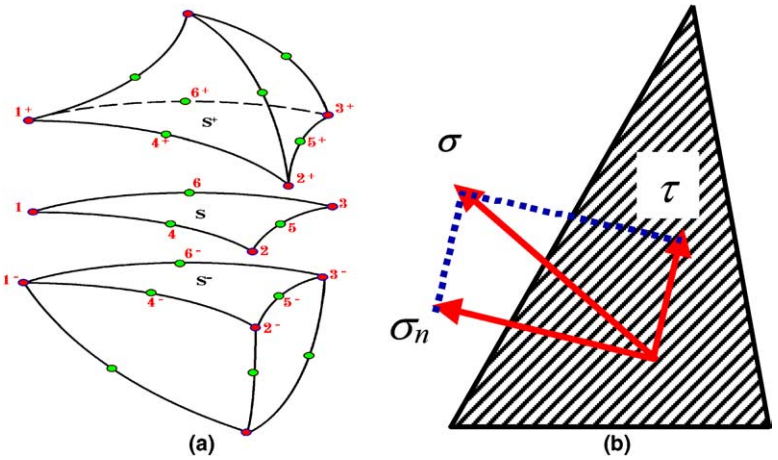

Fig. 3. (a) Cohesive element connecting two tetrahedral elements; (b) forces applied on a facet.

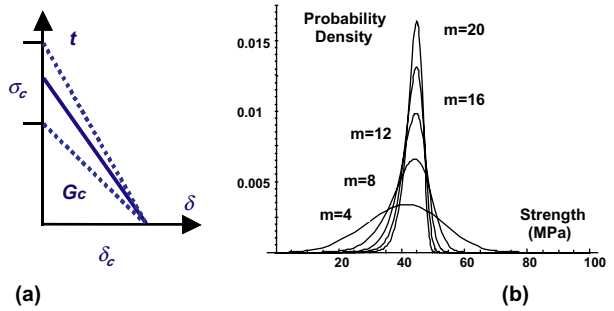

Fig. 4. (a) Local cohesive law; (b) Weibull distributions of microscopic strengths.

properties of ceramics, we assume that $\delta_{\text{facet}} = \delta_{\text{c}}$ throughout the material, while σ_{facet} is randomly distributed. The local cohesive law is illustrated in Fig. 4a. Therefore, a location with smaller σ_{facet} value represents a weaker or damaged point of the material, while a location with larger σ_{facet} value represents stronger, defect-free material.

Similar to Weibull's statistical strength theory (Weibull, 1939a,b, 1951), we propose a modified microscopic facet-strength distribution. At this distribution, the probability of a facet to break under effective tensile loading σ is:

$$P(\sigma) = 1 - \exp\left[-\left(\frac{A_{\text{facet}}}{A_{\text{s}}}\right)^{\frac{m_{\text{s}}}{m_{\text{a}}}} \left(\frac{\sigma}{\sigma_{\text{s}}}\right)^{m_{\text{s}}} \right] \tag{23}$$

where A_{facet} is the area of the facet, A_{s} is the scaling area; σ_{s} the scaling stress, m_{s} the Weibull modulus of strength distribution, and m_{a} the Weibull modulus for the effective area modification. From (23), the distribution of the local facet strength σ_{facet} is expressed by:

$$f(\sigma_{\text{facet}}) = \frac{\mathrm{d}P}{\mathrm{d}\sigma_{\text{facet}}} = \frac{m_s}{\sigma_s}\left(\frac{A_{\text{facet}}}{A_s}\right)^{\frac{m_s}{m_a}}\left(\frac{\sigma_{\text{facet}}}{\sigma_s}\right)^{m_s-1}\exp\left[\left(\frac{A_{\text{facet}}}{A_s}\right)^{\frac{m_s}{m_a}}\left(\frac{\sigma_{\text{facet}}}{\sigma_s}\right)^{m_s}\right] \tag{24}$$

As aforementioned, we assume that all the cohesive elements have the same critical opening distance, $\delta_{\text{facet}} = \delta_c$. For the convenience of statement, the value of δ_c is converted into the equivalent fracture energy, G_c, by:

$$G_c = \frac{\sigma_s \delta_c}{2} \tag{25}$$

Although the fracture energy may vary with location, the G_c value provides a measure of the material's average ductility.

Fig. 4b shows typical Weibull distributions. The smaller Weibull modulus (m), the broader the distribution becomes, and the material is more heterogeneous. On the other hand, larger m value represents a homogeneous material in which the local strength is almost constant.

Note that, in Eqs. (23) and (24), there exist two sets of Weibull parameters: the modulus and scaling stress for strength distribution $\{m_s, \sigma_s\}$, and the modulus and scaling area for effective facet area $\{m_a, A_s\}$. The first parameters set represents the statistical distribution of the defects within the material. The second parameters set represents the equivalent geometry effect originated from the characteristics of the facet dimensions. The physical meaning of the equivalent area is that a larger facet has more chance to contain defects, and therefore is more prone to fail. In other words, it has a lower strength and lower fracture energy. Note that it differs from the classical Weibull theory; m_a is not necessarily equal to m_s. We will see in the next section that the second parameters set helps to modify the unwanted mesh-dependency.

3.3. Physical problem

The specimen is a ceramic block, with dimensions $L_x = 1.5$ mm, $L_y = 0.5$ mm, and $L_z = 2.5$ mm. The specimen is loaded in z-direction by boundary velocities $v(t)$. The function of $v(t)$ is:

$$v(t) = \begin{cases} v_0 t/t_0, & t \leqslant t_0 \\ v_0, & t > t_0 \end{cases} \tag{26}$$

where $t_0 = L_z/c_L$ is the time that the stress wave needs to propagate a specimen length, $c_L = \sqrt{E/\rho}$ is the uniaxial stress wave velocity. Although very small, the speed ramp ($0 \sim t_0$) prevents the stepwise increasing boundary force, therefore smoothens the history curve of the boundary force. After t_0, the prescribed boundary velocity is kept at the constant value v_0. The strain-rate of the specimen is constant for $t > t_0$, as:

$$\dot{\varepsilon}_0 = 2v_0/L_Z \tag{27}$$

Along with the specimen's deformation, the forces applied on the two end surfaces of the specimen increase. Depending on the stress level and the local strength, an internal facet will be activated to form a cohesive element when the criterion (22) is satisfied. At the time the specimen fails catastrophically, the boundary force drops suddenly. The average value of the two peak boundary stresses is taken as the strength of the material. Because of the randomness, the strength of the specimen may be different from simulation to simulation, even for the same set of material parameters. To capture the statistical data of the specimen strength, Monte-Carlo simulations are performed. For each simulation case (fixed mesh, material parameters, and loading velocity), six numerical tests are performed. In each simulation the random seed is changed. Therefore, in one simulation the local strength at certain location is different from that in another simulation. Because the failure system is stochastic, this will result in different specimen strengths. The average value and the standard deviation of the six calculated strengths are taken as the characteristic strength values for this specific case.

The material is assumed to be hot-press densified silicon carbide (SiC–N). The material has density $\rho = 3200$ kg/m^3, Young's modulus $E = 460$ GPa, Poisson ratio $v = 0.16$. From this data, we can calculate the elastic wave speeds, as: uniaxial stress wave speed $c_L = 12{,}000$ m/s, shear wave speed $c_S = 7870$ m/s, and Rayleigh surface wave speed $c_R = 7160$ m/s. For the cohesive model, we take $\beta = 5.0$. For the statistical fracture model, the scaling stress is $\sigma_s = 415$ MPa, the scaling area is $A_s = 0.013$ mm^2. Unless stated otherwise in the text, we assume the Weibull modulus of the local strength distribution, m_s, to be 11.0. This is a typical value for densified silicon carbides (http://www.cercominc.com/scb.htm). Other material parameters, such as the fracture energy G_c, the loading speed, etc. will be changed in the following sections to show their influence on the deformation/failure properties of the specimen.

4. Addressing mesh-dependency

4.1. FEM meshes

We have constructed four meshes for the ceramic block. In each model the sizes of the tetrahedral elements are uniform. These meshes are shown in Fig. 5: from the coarsest to the finest, the element sizes R_{elem}, defined as the average length of the tetrahedral edges, are 0.25, 0.15, 0.10 and 0.075 mm, respectively. The statistics of these meshes are collected in Table 1. The two fine meshes ($R_{elem} = 0.10$, 0.075 mm) contain more than 14,000 internal facets, therefore are considered adequate for simulating the phenomenon of multiple cracks formation.

In the following part of this section, we will use these four meshes to demonstrate the unwanted mesh-dependency, and show an effective method of addressing it. The boundary velocity v_0 is fixed to 0.25 m/s, which is equivalent to the strain-rate $\dot{\varepsilon}_0 = 200$ 1/s.

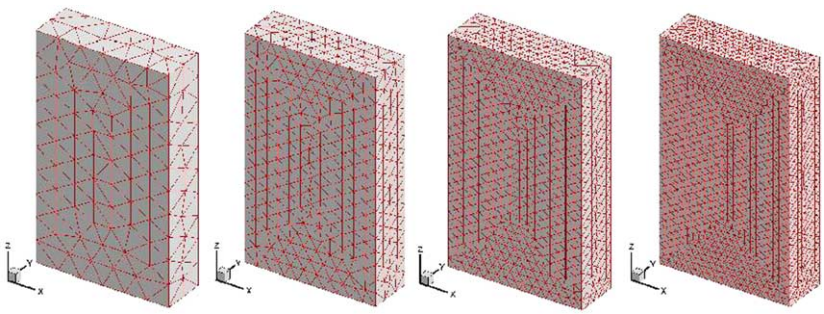

Fig. 5. FEM mesh of the ceramic block: $R_{elem} = 0.25$, 0.15, 0.10 and 0.075 mm.

Table 1
Statistics of four FEM meshes

Mesh type	Average mesh size (mm)	Total nodes	Total elements	Total facets	Total internal facets	Average facet area (mm^2)
Coarsest	0.25	1386	714	1229	497	0.038
Coarse	0.15	6085	3626	6656	4144	0.01268
Fine	0.1	17019	10719	20117	14325	0.00611
Finest	0.075	39464	25995	49634	38947	0.00336

4.2. Addressing mesh-dependency for brittle systems

For this material, the average fracture energy, G_c, is assumed to be 1.0 N/m. From (25) we can calculate, $\delta_c = 4.82$ nm, which is very small, meaning that the material is very brittle. For this system, we calculate the strength of the specimen using different meshes.

As a first simulation, we turn off the equivalent facet area term. This is done by assuming a very large value of m_a $(= 10^{12})$. According to (27), this means that the facet areas do not influence their strength. The strength distributions within the specimen are shown in Fig. 6a. The four distributions have maximum values at the identical stress level. The calculation specimen strength are shown in Fig. 6b. A significant mesh-dependency phenomenon is observed: the finer the mesh is, the weaker the ceramic block appears.

This observed mesh-dependency could be explained by the "weakest link" theory for brittle materials. As illustrated in Fig. 7, let us consider a one-dimensional case: a brittle bar is loaded by tensile force. Upon simulation, the bar is divided by a coarse mesh and a fine mesh. Since the material is very brittle, the failure of one element causes the complete failure of the bar. If the failure probabilities of a small element and a large element are identical, then, the fine mesh will render a weaker bar strength. The reason is simple: it contains more elements and has a larger chance of having weak ones among them.

To address this problem, it is necessary to introduce another length scale referred to as the equivalent length. The equivalent length modifies the failure probability of the elements with different lengths, so that the longer element has a larger probability to break.

For the three-dimensional failure problem, the "equivalent length" concept in the bar problem is extended to other equivalent geometric dimensions (equivalent length or volume). In our micro-cracking model where the failure of the specimen is caused by the breaking of internal facets, an "equivalent facet area" A_{facet} is introduced, which is explicitly expressed in Eqs. (23) and (24). As mentioned above, the Weibull modulus for the effective area, m_a, is not necessarily equal to the Weibull modulus of the strength m_s. Depending on the complexity of the problem (specimen geometry, material ductility, etc.), m_a values may be varied. This gives us additional freedom to simulate different problems.

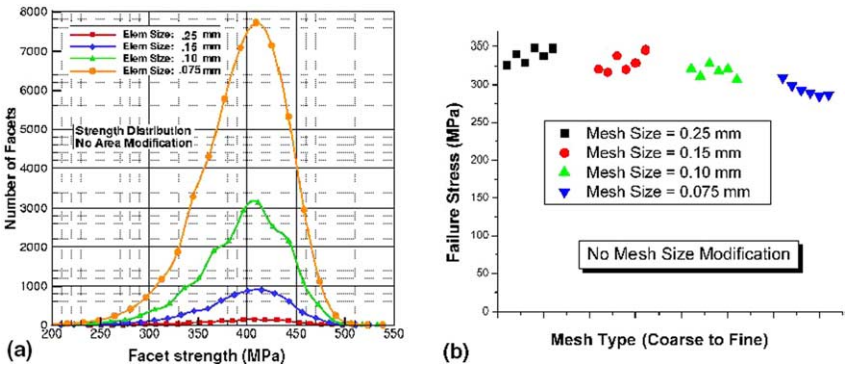

Fig. 6. (a) Facet strength distributions without area modification; (b) calculated brittle strengths.

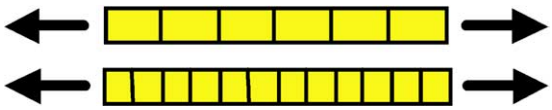

Fig. 7. A bar under tensile loading: a fine mesh renders a low strength if the failure probability is kept constant for different meshes.

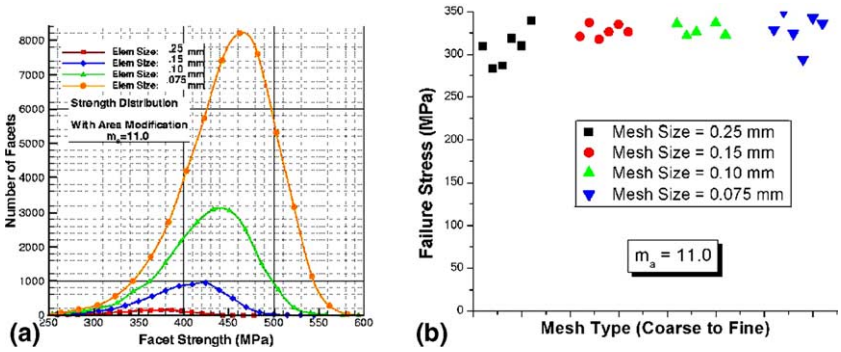

Fig. 8. (a) Facet strength distributions ($m_a = m_s = 11.0$); (b) calculated brittle strengths.

To address the unwanted mesh-dependency shown in Fig. 6b, we let the microscopic strength distribution be modified by facet area. Taking $m_a = m_s = 11.0$, the distributions are shown in Fig. 8a. It is seen that the distribution is different for different mesh size. The strength of a finer mesh (with smaller elements and facets) is higher. The results of the calculation are shown in Fig. 8b. Now the new calculated strengths converge to a constant value. The unwanted mesh-dependency is thus corrected.

4.3. Addressing mesh-dependency for ductile systems

Now consider a different material, whose fracture energy is taken to be $G_c = 50$ N/m. From (25) we can calculate, $\delta_c = 24.1$ nm, which is relatively larger. The material is ductile compared to the previous material type.

We calculate the strength of the specimen using different meshes. First we turn off the equivalent facet area term. The calculated specimen strengths are shown in Fig. 9a. Although we still observe the phenomenon of mesh-dependency (the finer mesh renders lower strengths), this tendency is less significant than the brittle system. If we continue to use the facet area modification with $m_a = 11.0$ ($m_a/m_s = 1$), the calculation specimen strengths exhibit a "reversed" mesh-dependency: a fine mesh renders a higher strength. This means that the unwanted mesh-dependency has been over-corrected.

Choosing a larger m_a value gives a weaker modification. For the present system, we found that the choice $m_a/m_s = 4$ renders good results. The calculated specimen strengths with the new m_a value are shown in

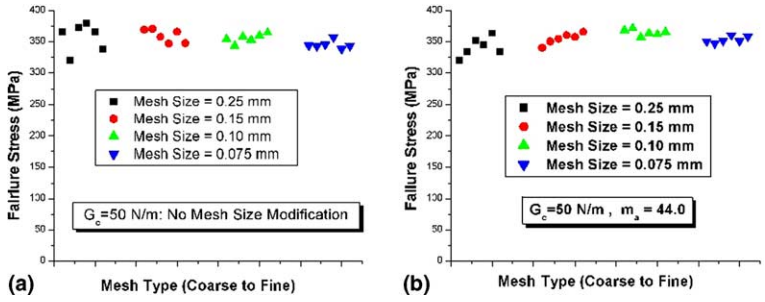

Fig. 9. Strengths of the ductile material: (a) without area modification, minor mesh-dependency is seen; (b) mesh-dependency is effectively corrected with a weak area modification ($m_a/m_s = 4$).

Fig. 9b. Clearly different meshes produce constant specimen strengths. This means that the mesh-dependency is mostly eliminated.

4.4. A discussion about mesh-dependency and its correction

We have considered two kinds of systems: a brittle system, and a ductile system. The difference appears in the material's fracture energy, G_c (for the brittle system, $G_c = 1$ N/m; for the ductile system, $G_c = 50$ N/m). For the brittle system, we showed that a significant mesh-dependency exists: the calculated specimen strength decreases when the mesh becomes finer (Fig. 6b). To solve this problem, we have introduced a mesh-dependent cohesive model. The modification Weibull modulus, $m_a = 11.0$, gives good correction results (Fig. 8b). On the other hand, for the ductile system, while the mesh-dependency effect still exists, it is not so significant (Fig. 9a). Accordingly, a weak modification, where the modification Weibull modulus, $m_a = 44.0$, is applied. This gives quite satisfactory results (Fig. 9b).

The reason for the differences can be explained using a mesh-size scale/cohesive-zone scale argument. The length scale of the cohesive zone ahead of a crack tip, R_{cohesive}, can be estimated by the following formula (firstly given by Rice in (1980) and restated by Falk et al. (2001)):

$$R_{\text{cohesive}} = \frac{9\pi}{32}\frac{E}{1-\nu^2}\frac{G_c}{\sigma_0^2} \tag{28}$$

Since $E = 460$ GPa, $\nu = 0.16$, $\sigma_0 \sim 415$ MPa, the scales of the cohesive zones are 0.0024 and 0.12 mm, for brittle and ductile materials, respectively.

In our four meshes, the length of the elements varies between 0.075 and 0.25 mm, which has the same order as the cohesive-zone scale of the ductile material (0.12 mm). When the mesh becomes finer, the physical features of fracture are better captured by these meshes. So the mesh-dependency is insignificant and a slight modification can correct it. We can assess that for a very ductile system (e.g. $G_c > 200$ N/m, $R_{\text{cohesive}} > 0.48$ mm), area modification is unnecessary and we can choose m_a to be infinite.

On the other hand, the cohesive-zone scale of the brittle material is 0.0024 mm, which is one to two orders less than our smallest element sizes. In this sense, the material is too brittle for our four meshes to resolve, and the fracture of the block basically observes "the weakest link" hypothesis. As illustrated in Fig. 7, a significant mesh-dependency is observed for this very brittle system. A modification based on Weibull theory should be used to correct this phenomenon. In essence, our calculations illustrate that, introducing an additional length scale into our Weibull distributed cohesive elements improves numerical results. Our model can be used in simulations in which a fine mesh may not be affordable at all locations.

Based on the above discussions, we conclude that the Weibull model takes its full meaning for low value G_c (brittle) materials.

5. Influence of material parameters

In this section, we will only use the second finest mesh ($R_{\text{elem}} = 0.10$ mm). The strain-rate is fixed to 200 s^{-1}. We also assume that $m_a/m_s = 1$ in all simulations. Unless otherwise stated, the Weibull modulus is $m_s = 11.0$; the fracture energy is $G_c = 1$ N/m We will exclusively vary m_s or G_c around the default values to investigate their effects on the specimen's failure properties.

5.1. Influence of Weibull modulus: m_s

All other parameters fixed, we change the Weibull modulus of microscopic strength distribution, as $m_s = 2.5, 5.5, 11.0, 20.0$. The microscopic strength distributions are shown in Fig. 10, where a smaller m_s

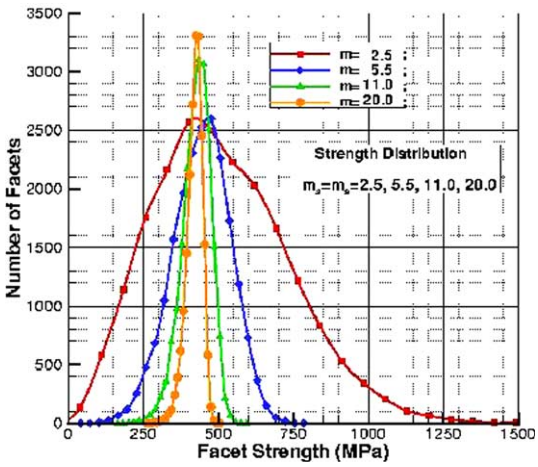

Fig. 10. Microscopic strength distributions ($m_s = 2.5$, 5.5, 11.0, and 20.0).

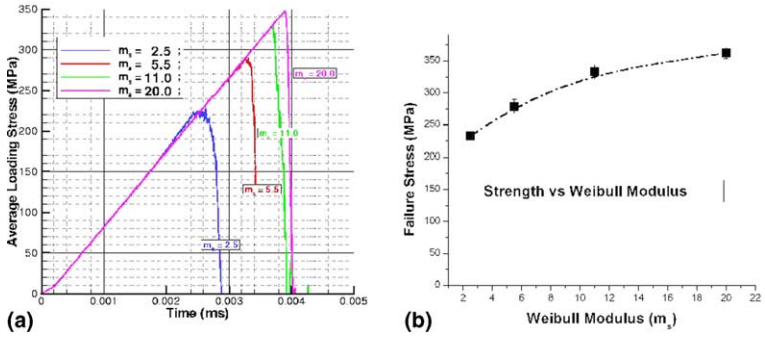

Fig. 11. (a) Loading histories for materials with different m_s values; (b) mean strengths and standard deviations of specimen strength vs. m_s values.

value produces a broader strength distribution, and physically represents a more heterogeneous material. Fig. 11a shows typical history curves of the loading stress. It is seen that for a small m_s value material, the loading curve appears rough before peak stress is reached. The reason is: this material has a broader strength distribution; therefore before the catastrophic specimen failure, the formation of the micro-cracks is relatively faster than that of a more homogeneous material.

The average specimen strengths are plotted against m_s value in Fig. 11b. It is seen that the specimen's failure strength increases with the Weibull modulus of the microscopic strengths. The reason is: at lower Weibull modulus, the material is more heterogeneous and there are more internal defects that can be activated at low stress levels; these micro-cracks make the specimen weaker. This dependency is the same to that observed in the compressive behavior (Zhou and Molinari, 2003).

5.2. Influence of fracture energy: G_c

In this section, the Weibull modulus of microscopic strength distribution is held constant at $m_s = 11.0$. The fracture energy G_c takes the values $G_c = 1.0$, 5.0, 10.0, 25.0, 50.0, 100.0, and 200.0 N/m. Note that even

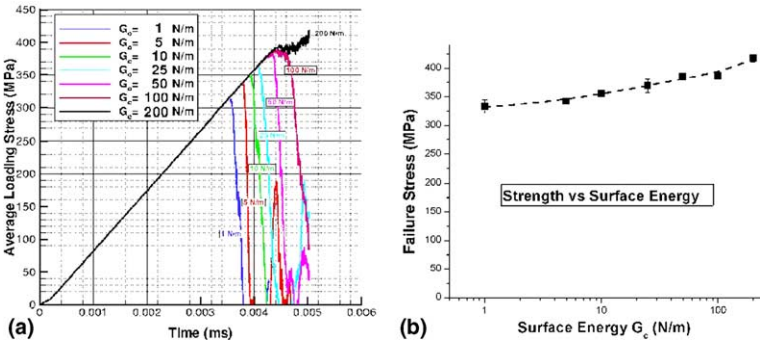

Fig. 12. (a) Loading histories for materials with different G_c values; (b) mean strengths and standard deviations of specimen strength vs. G_c values.

though G_c varies, we do not alternate m_a value, which is fixed to 11.0. The strength distribution, therefore, is fixed and shown in Fig. 8a or Fig. 10 (triangles). This helps us in comparing the specimen strength that is exclusively influenced by the G_c value.

According to (28), the length of the cohesive zone is $R_{cohesive} = 0.0024$, 0.012, 0.024, 0.06, 0.12, 0.24, and 0.48 mm, respectively. As the average mesh size is fixed to $R_{elem} = 0.10$ mm, the materials with $G_c \leqslant 25$ N/m appear to be brittle, while the materials with $G_c \geqslant 50$ N/m appear to be ductile in the simulations.

Fig. 12a shows typical histories of the loading stress. As expected, the failure properties of the larger G_c materials are more ductile; namely, the loading curves have longer non-linear regions prior to ultimate failure. This phenomenon is especially manifested by the material with $G_c = 200.0$ N/m, which does not show catastrophic stress drop. The calculated strengths are shown in Fig. 12b. It is seen that the failure strength of the specimen increases with fracture energy. The reason is that with a higher fracture energy, the activated micro-cracks within the specimen are more difficult to expand to cause a catastrophic specimen failure, therefore the specimen appears stronger. This tendency is also observed in the compressive strength of the materials (Zhou and Molinari, 2003).

Although it may not be significant, we have noticed that for the materials with higher fracture energy, the scatter of their failure strengths is smaller. The reason of this phenomenon will be discussed in details in the next section.

6. Failure of ceramics under dynamical loading

In this section, we use the mesh $R_{elem} = 0.10$ mm to investigate the dynamic failure characteristics of the ceramics. Two systems, a brittle one ($G_c = 1$ N/m, $m_a = m_s = 11.0$) and a ductile one ($G_c = 50$ N/m, $m_a = 44.0$, $m_s = 11.0$), are considered. The microscopic strength distributions for these two materials are shown in Fig. 13a. In Fig. 13a each distribution curve consists of three curves that come from three simulations. Note that the brittle system is a little stronger than the ductile system, as a result of mesh-dependency correction.

In the simulations of this section, all the material parameters are fixed at the default values, while the loading velocity v_0, and therefore the strain-rate $\dot{\varepsilon}_0$, vary. The prescribed boundary velocity curves are shown in Fig. 13b, the target v_0 are 0.05, 0.25, 1.25, 2.5, 6.25, 12.5, 25.0, and 50.0 m/s, respectively. This renders the target strain-rates to be 40, 200, 1000, 2000, 5000, 10,000, 20,000, and 40,000 s^{-1}, respectively.

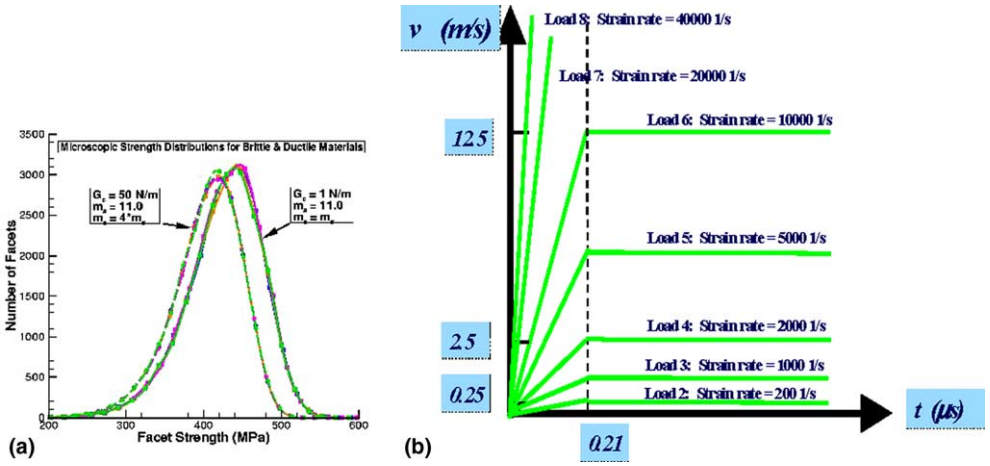

Fig. 13. (a) Strength distributions of the brittle system ($m_s = 11.0$, $m_a/m_s = 1.0$) and the ductile system ($m_s = 11.0$, $m_a/m_s = 4.0$); (b) prescribed boundary velocities.

6.1. Dynamic strengths

Under different loading rates, the typical loading stress curves are shown in Fig. 14. Although the curves shown are for a brittle system, the curves for the ductile system are similar. The curves generally reveal the brittle properties of the failure process: each stress increases linearly with time, and drops suddenly upon failure. For the very quick loading rate cases ($v_0 > 12.5$ m/s, or $\dot{\varepsilon}_0 > 10000\ s^{-1}$), the specimen breaks before the target velocity v_0 is reached. Therefore, the target strain-rates $\dot{\varepsilon}_0$ are not reached. In these cases, we take the *maximum* loading speed v_{max} (boundary velocity at the breaking time) to calculate the real strain-rates.

The calculated specimen strengths (the average value and the standard deviations) are plotted against the logarithm of the real strain-rates in Fig. 15. It is seen that for both materials, the failure strength of the specimen increases with the strain-rates. This differs from our previous simulating results on compressive strengths (Zhou and Molinari, 2003). Since the crack initiation criterion and the cohesive model are not

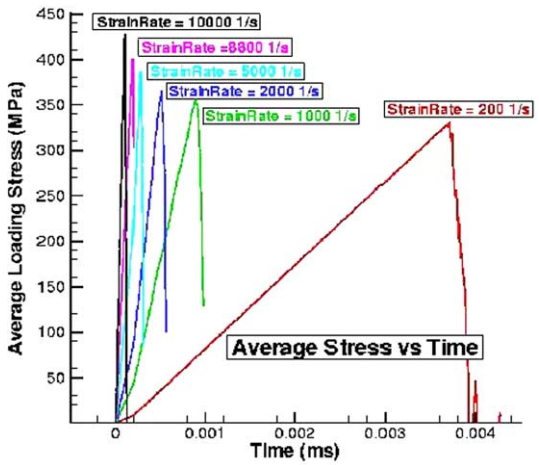

Fig. 14. Loading histories of brittle system ($G_c = 1$ N/m) under different strain-rates.

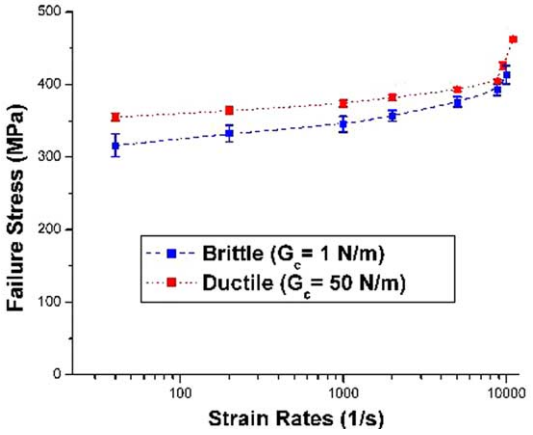

Fig. 15. Average strengths and strength scatters of brittle and ductile materials.

rate-dependent, the observed strain-rate-dependency of specimen strength comes from inertial effect and/or from the micro-cracking mechanism. Detailed discussions about the rate-dependency will be made in the next part of this section.

Besides the rate-dependency, we observe the following phenomena:

(1) As mentioned in 5.2, the ductile system ($G_c = 50$ N/m) has higher failure strength than the brittle system ($G_c = 1$ N/m). This is true even though the brittle material has a stronger microscopic strength distribution (see Fig. 13a). This is explained as follows: the fracture energy of a ductile system is higher than that of a brittle system. Therefore, the activated micro-cracks within the ductile specimen are more difficult to expand to cause a catastrophic specimen failure, hence a higher apparent strength level for the ductile specimen.
(2) For a ductile system, the scatter of the failure strengths is much less than that for a brittle system. This phenomenon can be explained by the ductility of the material. When the material has low fracture energy, the specimen is so brittle that one or a few weak points (the micro-cracks activated at defect locations) may cause catastrophic specimen failure, therefore the material strengths are governed by the stochastic distributions of these weak points. The weakest link hypothesis is more applicable to such brittle system. On the other hand, the failures of ductile materials are more controlled by the collective behavior of many cracks, which are less stochastic due to the averaging effect. As a result, the failure strengths of this ductile system are less scattered.
(3) Even for the brittle system where strength scatters are large, the level of scatter tends to decrease with the strain-rate. In other word, the material appears less stochastic at higher strain-rate. The reason for this is: at a higher deformation rate, more micro-cracks are activated at the specimen failure (see the next section). This large number of the activated micro-cracks results in more averaging effect, thus decreases the material's stochasticity.

6.2. On the rate-dependency of the tensile strengths

In this part, we discuss in details the observed rate-dependency of the specimen strength. As shown in Fig. 15, both materials exhibit remarkable rate-hardening effects. The rate-dependency is more significant at higher strain-rates ($d\varepsilon/dt > 5000\ s^{-1}$) than at lower strain-rates ($d\varepsilon/dt = 40$–$5000\ s^{-1}$). In lower strain-rate region, the rate-hardening effect for a ductile material is less than that for a brittle material.

Since in our model the crack initiation criterion and the cohesive model are not rate-dependent, the apparent strain-rate-hardening effect comes exclusively from inertial effects. There exist two forms of inertial influences: *structural inertia* and *inertia related micro-cracking*. The two effects are discussed in details below.

(1) *Structural inertia*: at very high strain-rates: $\dot{\varepsilon}_0 > 5000\ s^{-1}$ (here $\dot{\varepsilon}_0$ is the real strain-rate), the apparent rate-hardening tendency is mainly attributed to the effect of stress wave propagation within the specimen. In these cases, the target strain-rates are 10,000, 20,000 and 40,000 s^{-1}. However, the specimen breaks before the target strain-rate is reached. To mend this problem we calculate the real strain-rate with the boundary speed at failure point, which gives values of 8860, 9550 and 11,000 s^{-1}, respectively. Further, as the fracture happens before the stress wave propagates to the other side of the specimen, the stress distribution within the specimen is not uniform at failure point. Therefore, the failure strength, taken as the boundary stress, is only of relative meaning. The sudden increase of the rate-dependency is only reflected in these non-uniform loading cases.
(2) *Micro-cracking effect*: The specimen failure is caused by micro-cracks initiation and propagation. Because the extension of the micro-cracks takes time, other micro-cracks may be activated before a neighboring activated micro-crack extends and unloads them. As a result, the block breaks with more

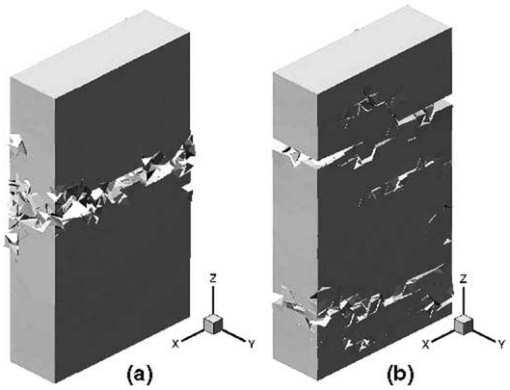

Fig. 16. Typical failure pattern of brittle specimen: (a) $\dot{\varepsilon}_0 = 200\ s^{-1}$; (b) $\dot{\varepsilon}_0 = 1000\ s^{-1}$.

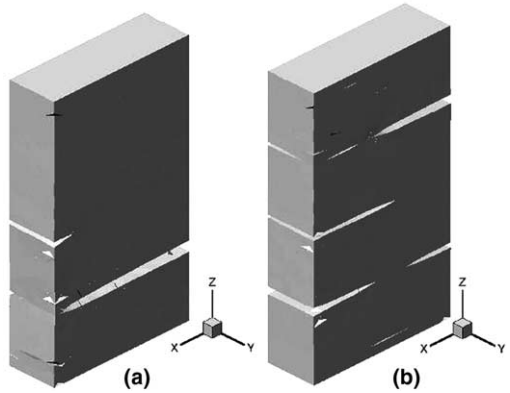

Fig. 17. Typical failure pattern of ductile specimen: (a) $\dot{\varepsilon}_0 = 200\ s^{-1}$; (b) $\dot{\varepsilon}_0 = 1000\ s^{-1}$.

cracks at higher loading rates; while at lower loading rates, a single main crack may cause catastrophic block failure. This phenomenon is manifested in Fig. 16 for the brittle system ($G_c = 1$ N/m), where the specimen fails with one or two main cracks under 200 s^{-1} strain-rates (Fig. 16a), but fails with three or more main cracks under 1000 s^{-1} strain-rates (Fig. 16b). This failure pattern difference devotes to the observed strain-rate effects, especially in the relatively low strain-rate region ($\dot{\varepsilon}_0 > 40$–5000 s^{-1}).

The same tendency exists in the ductile material ($G_c = 50$ N/m), but seems less significant. The typical failure patterns of ductile specimens are shown in Fig. 17. Because the material is very ductile, at a low strain-rate a few occasionally activated micro-cracks are not enough to cause catastrophic block failure. Therefore the aforementioned failure pattern difference is less significant than that in the brittle case. This explains the observation that in the region $\dot{\varepsilon}_0 = 40$–5000 s^{-1} the rate-hardening effect is weaker with increasing ductility.

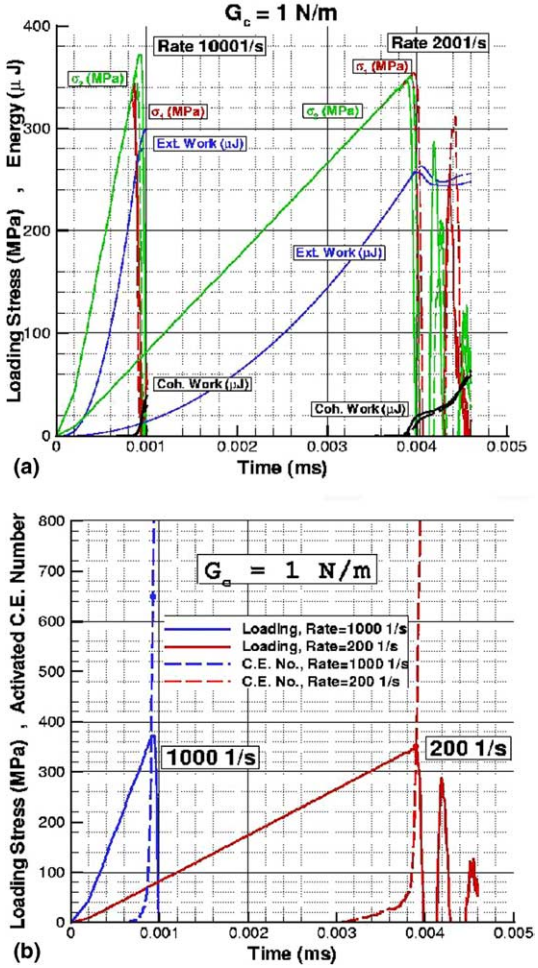

Fig. 18. History curves of brittle materials ($G_c = 1$ N/m): (a) loading forces/energy quantities vs. time; (b) loading forces/nucleated CE number vs. time.

Table 2
Failure parameters for brittle specimen

	Brittle $G_c = 1$ N/m	
	$\dot{\varepsilon}_0 = 200\ s^{-1}$	$\dot{\varepsilon}_0 = 1000\ s^{-1}$
Failure stress (MPa)	345	368
Activated cohesive element	350	650
Cohesive energy dissipation (μJ)	6.2	18
Percent of energy dissipation	2.5%	6%

Table 3
Failure Parameters for Ductile Specimen

	Ductile $G_c = 50$ N/m	
	$\dot{\varepsilon}_0 = 200\ s^{-1}$	$\dot{\varepsilon}_0 = 1000\ s^{-1}$
Failure stress (MPa)	355	380
Activated cohesive element	240	460
Cohesive energy dissipation (μJ)	22	56
Percent of energy dissipation	8.6%	17%

Additionally, we have quantitatively investigated the *micro-cracking* process of tensile failure. We plot the history curves of the loading-stress, the activated cohesive-elements number, the dissipated cohesive energy, and the total external work provided into the system. Fig. 18 shows these curves for a brittle system ($G_c = 1$ N/m). The failure time is defined as the time when the external loading drops suddenly. After failure, the stress within the specimen is released by the newly formed crack surface. Because the fracture process is very fast, the stress release is accompanied by stress wave reflections within the broken pieces, causing external loading oscillations and temporary compressive stress. The micro-cracking parameters at the failure point are measured directly from the other history curves. These data are collected in Table 2. These data show that, at failure, more cohesive elements are activated in the higher strain-rate case than in the lower strain-rate case. As a result, more cohesive energy is dissipated at failure when the strain-rate is higher. Such difference is in agreement with the failure patterns shown in Fig. 16. The more dissipated cohesive energy at higher strain-rate case results in phenomenological rate-dependency of the failure strength.

A similar calculation is performed for the ductile material ($G_c = 50$ N/m). The history curves are omitted due to the length limitation of this paper. Typical failure parameters of the ductile material are collected in Table 3. Similar to the brittle case, at the failure point of a ductile material, more cohesive elements are nucleated, and more cohesive energy dissipated when the loading rate is higher. This phenomenon qualitatively agrees with the failure pattern observations (Fig. 17). The increased cohesive energy dissipation devotes to the phenomenological strength rate-dependency.

Summarizing the above results, we conclude that for a high loading rate case, more micro-cracks are initiated at the failure point, and more energy is dissipated. This tendency exists for both brittle and ductile material. This mechanism results in the rate-dependency of the specimen strength. Due to the averaging effect, it also causes the specimen strength to be less scattered at high strain-rate.

7. Conclusions and discussion

In this paper, we have numerically simulated the dynamic fracture process of a ceramic block under tensile loading. The simulation was performed using an explicit dynamic finite element method. The ceramic material was considered as two parts: the bulk material regions discretized by tetrahedral elements,

and the internal micro-cracks that appear at the interfaces (facets) between ordinary elements (Fig. 2b). The constitutive law for the bulk material was linear, homogeneous, isotropic elasticity; while the mechanical behaviors of the micro-cracks were described by cohesive elements.

A stochastic micro-cracking model considering the random distribution of internal defects in the material was proposed. Upon loading, micro-cracks nucleated randomly in the block, which grew and coalesced with each other causing the catastrophic failure of the specimen. The micro-cracking model consists of a Weibull distribution of the local strengths (strength Weibull), and a facet area modification (geometry Weibull) that accounts for the equivalent geometry of the damaged material (Eqs. (23) and (24)).

We have considered a brittle system and a ductile system to investigate the mesh-dependency of the model. The fracture properties of the material were simulated by using four different meshes (Fig. 5). For the brittle system, we found that if the geometry Weibull was not included in the model, then due to the "weakest link phenomenon", the specimen appeared weaker at finer meshes. Namely, the calculation results are mesh-dependent (Fig. 6b). By using a Weibull type equivalent area modification with geometry Weibull modulus $m_a = m_s$, the unwanted mesh-dependency was effectively eliminated (Fig. 8b). For the ductile system without geometry modification, the mesh-dependency still existed but was less significant (Fig. 9a). Accordingly, a weak modification with $m_a = 4m_s$ rendered satisfactory results (Fig. 9b). Therefore a modified Weibull model is important for brittle materials.

Parametric studies were performed to investigate the influence of material properties on the structural strength. We showed that the failure strength of the specimen increases with the fracture energy (G_c), Fig. 12b. The reason is that at higher G_c, the material is very ductile and the activated micro-cracks are more difficult to expand. Additionally, we demonstrated that the failure strength of the specimen increases with the Weibull modulus of the microscopic strengths (m_s), Fig. 11b. The reason is: if m_s is lower, the material is more heterogeneous and contains more internal defects. The defects are activated as micro-cracks at lower stress level. As a result, the specimen becomes weaker.

Finally we have studied the failure properties of two material systems that are loaded at different loading rates. Both materials showed significant rate-hardening: the apparent specimen strength increases with the strain-rate (Fig. 15). Also we found that the scatter of the failure strengths is less than that for a brittle system (Fig. 15). Again these phenomena were explained by the micro-cracking mechanism of the materials. We showed that the failure of a brittle system is more controlled by its internal microscopic-scale weaker points under "the weakest link" hypothesis. Therefore at the macroscopic scale, the strength of the brittle specimen appears stochastic. On the other hand, the failure of a ductile system is controlled by the initiation and the (sticky) growth of many micro-cracks; the collective behavior of these micro-cracks smoothens down the randomness at the macroscopic scale.

The observed failure strength rate-dependency was explained by material's inertia. This inertial effect influences the fracture process of the specimen, either directly as stress wave propagation, or indirectly through the micro-cracking mechanism. We found that the micro-cracking mechanism is different for static loading and dynamic loading. When the specimen breaks under higher loading rate, more micro-cracks are nucleated because the adjacent already-nucleated cracks do not have enough time to unload each other. This is manifested by the numbers of the activated cohesive elements under different loading speed (Tables 2 and 3). The failure patterns have also illustrated this difference (Figs. 16 and 17). As a result, when a specimen is loaded at a higher speed, more cohesive energy is dissipated before its catastrophic failure. This energy increase is, at least partially, responsible for the apparent increase of the specimen strength.

This dynamic micro-cracking mechanism has been observed experimentally in the failure process of ceramics under impact compressive loading. Subhash and Ravichandran (2000) have pointed out that when the loading rate increases the time available for a crack to initiate and grow reduces. As a result, the inertia associated with crack-growth acceleration will inhibit early fracture while the applied stress continues to rise rapidly, elevating the compressive failure strength under dynamic loads. Wang and

Ramesh's work (2004) shows that the fragment sizes of SiC–N decreases with the compression strain-rate. Due to experimental difficulties, little direct measurements are available on the failure strength of ceramics under dynamic tensile loading. However, there are indirect experimental observations that show material break into many pieces under a rapid-applied tensile loading (Grady and Benson, 1983). The one-dimensional model based on stress wave propagation/interaction analysis has shown that under dynamic loading, the increasing of fragment number (and the decreasing of fragment size) are attributed to the material's inertia effect (Drugan, 2001). Numerical simulations also proved this (Pandolfi et al., 1999), though no failure strength data have been given. In our analysis, we have directly calculated the tensile strength of the material, and exhibit the rate-dependency explicitly. Our results are supported by the analysis of Denoual and Hild, which was carried out using a statistical fracture model (Denoual and Hild, 2000). Note that the Denoual and Hild's model also exhibits the tendency that the material's stochasticity decreases with loading rate (see detailed discussion in Hild et al., 2000), which is also shown in our observations.

The cohesive laws incorporated in the present analysis were rate-independent, with only two basic parameters: the microscopic strength σ_c and the fracture energy G_c. Nevertheless, in the case of dynamic loading, an intrinsic time scale exits in this model. As pointed out by Camacho and Ortiz (1996), the time scale, $t_c = \delta_c/c$, is linked to the critical cohesive opening displacement ($\delta_c = 2G_c/\sigma_c$) and the elastic stress wave velocity (c). It is shown that this simple, rate-independent cohesive model can describe many dynamic fracture/fragmentation phenomena. In our previous work, we have shown that a rate-independent cohesive law, in conjunction with a rate-dependent bulk material constitutive law, is able to simulate the rate-dependent dynamic fracture of ductile metallic materials (Zhou et al., 2004). The present work shows that, the rate-independent cohesive law, when combined with the dynamic micro-cracking (nucleation and growth) mechanism, which is closely related to material inertia, brings out a strong rate-dependency of the dynamic tensile strength.

It is noteworthy that the observed rate-dependency for the tensile failure is different from the case of compressive failure. When the specimen is compressed up to breaking, the failure strength shows quite small dependency (Zhou and Molinari, 2003). An explanation of this difference is that the compressive failure strength of SiC–N is typically 6 GPa, about 15 times the value of the tensile failure strength. At failure point, the strain energy density stored within a compressive specimen is more than 200 times larger than that stored in a tensile specimen. As a result, upon compressive failure, the share of the cohesive energy dissipation is negligibly small. Therefore, although there is a difference between the dynamic micro-cracking mechanism and the static one, the energy attributions are so small that the phenomenological rate-dependency is moderate for the compressive case.

Acknowledgements

The authors would like to thank Professor K.T. Ramesh of the Johns Hopkins University for his invaluable comments.

This work was performed under the auspices of the Center for Advanced Metallic and Ceramic Systems at Johns Hopkins. The research was sponsored by the Army Research Laboratory (ARMAC-RTP) and was accomplished under the ARMAC-RTP Cooperative Agreement Number DAAD19-01-2-0003 and under Rutgers University subcontract 1221. The views and conclusions contained in this document are those of the authors and should not be interpreted as representing the official policies, either expressed or implied, of the Army Research Laboratory or the US Government. The US Government is authorized to reproduce and distribute reprints for Government purposes not withstanding any copyright notation hereon.

References

Barrenblatt, G.I., 1962. The mathematical theory of equilibrium of cracks in brittle fracture. Adv. Apply. Mech. 7, 55–129.

Belytschko, T., 1983. An overview of semi-discretization and time integration procedures. In: Belytschko, T., Hughes, T.L.J. (Eds.), Computational Methods for Transient Analysis. North-Holland, pp. 1–65.

Bhattacharya, K., Ortiz, M., Ravichandran, G., 1998. Energy-based model of compressive splitting in heterogeneous brittle solids. J. Mech. Phys. Solids 46, 2171–2181.

Bourne, N., Millett, J., Rosenberg, Z., Murray, N., 1998. On the shock induced failure of brittle solids. J. Mech. Phys. Solids 46, 1887–1908.

Camacho, G.T., Ortiz, M., 1996. Computational modelling of impact damage in brittle materials. Int. J. Solids Struct. 33, 2899–2938.

Chen, W., Ravichandran, G., 1997. Dynamic compressive failure of a glass ceramic under lateral confinement. J. Mech. Phys. Solids 45, 1303–1328.

Chen, W., Ravichandran, G., 2000. Failure mode transition in ceramics under dynamic multiaxial compression. Int. J. Fracture 101, 141–159.

Denoual, C., Hild, F., 2000. A damage model for the dynamic fragmentation of brittle solids. Comput. Methods Appl. Mech. Engng. 183, 247–258.

Drugan, W.J., 2001. Dynamic fragmentation of brittle materials: analytical mechanics-based models. J. Mech. Phys. Solids 49, 1181–1208.

Dugdale, D.S., 1960. Yielding of steel sheets containing slits. J. Mech. Phys. Solids 8, 100–104.

Espinosa, H.D., Zavattieri, P.D., Dwivedi, S.K., 1998. A finite deformation continuum/discrete model for the description of fragmentation and damage brittle materials. J. Mech. Phys. Solids 46, 1909–1942.

Falk, M.L., Needleman A., Rice J.R., 2001. A critical evaluation of dynamic fracture simulations using cohesive surfaces. Presented at the 5th European Mechanics of Materials Conference, Delft, The Netherlands, 5–9 March 2001.

Grady, D.E., 1997. Shock-wave compression of brittle solids. Mech. Mater. 29, 181–203.

Grady, D.E., Benson, D.A., 1983. Fragmentation of metal rings by electromagnetic loading. Exp. Mech. 23, 393–400.

Hild, F., Denoual, C., Forquin, P., Brajer, X., 2000. On the probabilistic–deterministic transition involved in a fragmentation process of brittle materials. Comput. Struct. 81, 1241–1253.

Hughes, T.L.J., 1987. The Finite Element method: Linear Static and Dynamic Finite Element Analysis. Prentice-Hall, Englewood Cliffs, NJ.

Jiao, T., Li, Y., Ramesh, K.T., Wereszczak, A.A., 2004. High rate testing and dynamic failure of structural ceramics. Int. J. Appl. Ceram. Technol., in press.

Miller, O., Freund, L.B., Needleman, A., 1999. Modeling and simulation of dynamic fragmentation in brittle materials. Int. J. Fract. 96, 101–125.

Molinari, J.F., Ortiz, M., 2002. Three-dimensional adaptive meshing by subdivision and edge-collapse in finite-deformation dynamic-plasticity problems with application to adiabatic shear banding. Int. J. Numer. Methods Engng. 53, 1101–1126.

Ortiz, M., Pandolfi, A., 1999. Finite-deformation irreversible cohesive elements for three-dimensional crack propagation analysis. Int. J. Numer. Methods Engng. 44, 1267–1286.

Pandolfi, A., Ortiz, M., 2002. An efficient adaptive procedure for three-dimensional fragmentation simulations. Engng. Comput. 18, 148–159.

Pandolfi, A., Krysl, P., Ortiz, M., 1999. Finite element simulation of ring expansion and fragmentation: the capturing of length and time scales through cohesive models of fracture. Int. J. Fract. 95, 279–297.

Pandolfi, A., Guduru, P.R., Ortiz, M., Rosakis, A.J., 2000. Three dimensional cohesive-elements of dynamic fracture in C300 steel. Int. J. Solids Struct. 37, 3733–3760.

Ravichandran, G., Subhash, G., 1995. A micromechanical model for high strain rate behavior of ceramics. Int. J. Solids Struct. 32, 2627–2646.

Rice, J.R., 1980. The mechanics of earthquake rupture. In: Dziewonski, A.M., Boschi, E. (Eds.), Physics of the Earth's Interior, Proceedings of International School of Physics "Enrico Fermi". North Holland, pp. 555–649.

Ruiz, G., Ortiz, M., Pandolfi, A., 2000. Three dimensional finite-element simulation of the dynamic brazilian tests on concrete cylinders. Int. J. Numer. Methods Engng. 48, 963–994.

Ruiz, G., Ortiz, M., Pandolfi, A., 2001. Three dimensional cohesive modeling of dynamic mixed-mode fracture. Int. J. Numer. Methods Engng. 52, 97–120.

Sarva, S., Nemat-Nasser, S., 2001. Dynamic compressive strength of silicon carbide under uniaxial compression. Mater. Sci. Engng. A317, 140–144.

Shih, C.J., Meyers, M.A., Nesterenko, V.F., Chen, S.J., 2000. Damage evolution in dynamic deformation of silicon carbide. Acta. Mater. 48, 2399–2420.

Subhash, G., Ravichandran, G., 1998. Mechanical behaviour of hot pressed aluminum nitride under uniaxial compression. J. Mater. Sci. 33, 1933–1939.

Subhash, G., Ravichandran, G., 2000. Split-Hopkinson pressure bar testing of ceramics. In: ASM Handbook Mechanical Testing and Evaluation, vol. 8. ASM International, pp. 497–504.

Walter, M.E., Owen, D.W., Ravichandran, G., 1994. Static and dynamic tension testing of ceramics and ceramic composites. Mechanical Testing of Ceramics and Composites, AMD-Vol. 197.

Wang, H., Ramesh, K.T., 2004. Dynamical strength and fragmentation of hot-pressed silicon carbide under uniaxial compression. Acta Materialia 52, 355–367.

Weibull, W., 1939a. The phenomenon of rupture in solids. Proc. R. Swedish Inst. Engng. Res., 153.

Weibull, W., 1939b. A statistical theory of the strength of materials. Proc. R. Swedish Inst. Engng. Res., 151.

Weibull, W., 1951. A statistical distribution function of wide applicability. J. Appl. Mech. 18, 293–297.

Xu, X.-P., Needleman, A., 1994. Numerical simulations of fast crack growth in brittle solids. J. Mech. Phys. Solids 42, 1397–1434.

Xu, X.-P., Needleman, A., 1996. Numerical simulations of dynamic crack growth along an interface. Int. J. Fract. 74, 289–324.

Zavattieri, P.D., Espinosa, H.D., 2001. Grain level analysis of crack initiation and propagation in brittle materials. Acta. Mater. 49, 4291–4311.

Zavattieri, P.D., Raghuram, P.V., Espinosa, H.D., 2001. A computational model of ceramic microstructures subjected to multi-axial dynamic loading. J. Mech. Phys. Solids 49, 27–68.

Zhai, J., Zhou, M., 2000. Finite element analysis of micromechanical failure modes in a heterogeneous ceramic material system. Int. J. Fract. 101, 161–180.

Zhou, F., Molinari, J.-F., 2001. 3D finite element analysis of impact damage in metallic and ceramic targets. Symposium on Ceramic Armor Materials by Design, PACRIM 4, November 2001. Ceramic Transactions, vol. 134, pp. 317–327.

Zhou, F., Molinari, J.-F., 2004. Dynamic crack propagation with cohesive elements: a methodology to address mesh dependency. Int. J. Numer. Meth. Eng. 59, 1–24.

Zhou, F., Molinari, J-F., 2003. Numerical investigation of dynamic compressive loading. In: Proceedings of the 27th Annual Cocoa Beach Conference on Advanced Ceramics and Composites, Ceramic Engineering and Science Proceedings 24, 417–423.

Zhou, F., Molinari, J.-F., Li, Y., 2004. Three dimensional numerical simulation of dynamic fracture in silicon carbide reinforced aluminum. Eng. Fract. Mech. 71, 1357–1378.